Assessment of sulfur-functionalized MXenes for li-ion battery applications

C: Energy Conversion and Storage; Energy and Charge Transport

Assessment of Sulfur-Functionalized MXenes for Li-ion Battery Applications

Edirisuriya M. Dilanga Siriwardane, Ilker Demiroglu, Cem Sevik, Francois M. Peeters, and Deniz Cakir

J. Phys. Chem. C, **Just Accepted Manuscript** • DOI: 10.1021/acs.jpcc.0c05287 • Publication Date (Web): 01 Sep 2020

Assessment of Sulfur-functionalized MXenes for Li-ion Battery applications

Edirisuriya M. D. Siriwardane,[†] Ilker Demiroglu,[‡] Cem Sevik,[¶] François M. Peeters,[§] and Deniz Çakır*,[†]

†*Department of Physics and Astrophysics, University of North Dakota, Grand Forks, North Dakota 58202, USA*

‡*Department of Advanced Technologies, Eskisehir Technical University, 26555, Eskisehir, Turkey*

¶*Department of Mechanical Engineering, Faculty of Engineering, Eskisehir Technical University, Eskişehir, TR 26555, Turkey*

§*Department of Physics, University of Antwerp, Groenenborgerlaan 171, 2020 Antwerpen, Belgium*

E-mail: deniz.cakir@und.edu

Abstract

The surface termination of MXenes greatly determines the electrochemical properties and ion kinetics on their surfaces. So far, hydroxyl, oxygen, and fluorine-terminated MXenes have been widely studied for energy storage applications. Recently, sulfur functionalized MXene structures, which possess low diffusion barriers, have been proposed as candidate materials to enhance battery performance. We performed first-principles calculations on the structural, stability, electrochemical, and ion dynamic properties of Li adsorbed sulfur-functionalized group 3B, 4B, 5B, and 6B transition metal (M)-based MXenes (i.e., M_2CS_2 with M= Sc, Ti, Zr, Hf, V, Nb, Ta, Cr, Mo, and W). We performed phonon calculations, which indicate that all the above M_2CS_2 MXenes, except

for Sc, are dynamically stable at T = 0 K. The ground-state structure of each M_2CS_2 monolayer depends on the type of M atom. For instance, while sulfur prefers to sit at the FCC site on Ti_2CS_2, it occupies the HCP site of Cr-based MXene. We determined the Li adsorption configurations at different concentrations using the cluster expansion method. The highest maximum open-circuit voltages were computed for group 4B element (i.e., Ti, Zr, and Hf)-based M_2CS_2, which are larger than 2.1 V, while their average voltages are approximately 1 V. The maximum voltage for group 6B element (i.e., Cr, Mo, W)-based M_2CS_2 are less than 1 V, and the average voltage is less than 0.71 V. We found that S functionalization is helpful for capacity improvements over the O-terminated MXenes. In this respect, the computed storage gravimetric capacity may reach up to 417.4 $mAhg^{-1}$ for Ti_2CS_2 and 404.5 $mAhg^{-1}$ for V_2CS_2. Ta, Cr, Mo, and W-based M_2CS_2 MXenes show very low capacities, which are less than 100 $mAhg^{-1}$. The Li surface diffusion energy barriers for all the considered MXenes are less than 0.22 eV, which is favorable for high charging and discharging rates. Finally, *Ab*-initio molecular dynamic simulations performed at 400 K and bond length analysis with respect to Li concentration verify that selected promising systems are robust against thermally induced perturbations that may induce structural transformations or distortions and undesirable Li release.

Introduction

Rechargeable high energy storage is a major concern in technologies such as portable electronic devices and electric automobiles. Several different materials have been proposed to enhance storage capacity and cycling performance, but the desired goals could not be achieved yet. Two-dimensional (2D) materials have been vastly considered for Li-ion storage. The large surface areas on 2D sheets offer a higher number of electrochemically active sites to attract Li-ions.[1] Thus, a higher capacity can be realized by utilizing the 2D electrodes. 2D transition metal carbides, nitrides, and carbonitrides (MXenes) are appealing materials as

battery electrodes owing to their excellent electronic conductivity and stability.[2] The general chemical formula of MXenes is given as $M_{n+1}X_nT_x$, where M is an early transition metal, X represents C and/or N atom, and T is the surface termination group.[3] Bare MXenes surface is highly reactive and mostly functionalized by O, F, or OH.[4] O was found to be the most favorable termination group when compared to the F and OH cases for MXene.[5] In recent years, MXenes have garnered a growing interest as electrodes in energy storage applications, including batteries and super capacitors.[6–11]

Recently, sulfur functionalized MXenes have emerged as promising candidates as electrode materials because of their lower energy barriers, which offer higher charging/discharging rates and larger power densities.[4] Importantly, the successful synthesis of MXenes with O, NH, S, Cl, Se, Br, and Te terminations has been recently demonstrated.[12] The lightest MXene Ti_2C with S termination has been studied for Li, Na, K, Mg, and Ca intercalation, where energy barriers are less than 0.5 eV. Mg intercalated Ti_2CS_2 provides excellent gravimetric capacity (1871.13 $mAhg^{-1}$),[13] which is much greater than that from bare Ti_2C ($\approx$ 700 $mAhg^{-1}$) and Ti_2CO_2 (570 $mAhg^{-1}$) monolayers.[14] It has been reported that Na adsorbed $Ti_3C_2S_2$ nanosheets pose lower energy barrier (0.11 eV) than $Ti_3C_2O_2$ (0.22 eV).[15] S-functionalized V_2C also provides lower energy barriers for Li and Na as compared to O-functionalized V_2C.[4] Fe_2CS_2 MXene has been discovered as a suitable electrode material for Al-ion batteries. Fe_2CS_2 can provide a capacity of 642 $mAhg^{-1}$, which is more than twice the capacity from Fe_2CO_2 (288 $mAhg^{-1}$).[16] Considering the potential of these materials as electrode materials in battery applications, we carried out density functional theory (DFT) based calculations for M_2CS_2 MXenes, where M = Sc, Ti, Zr, Hf, V, Nb, Ta, Cr, Mo, and W. Our phonon calculations reveal that all the above MXenes, except Sc-based one, are dynamically stable. Cluster expansion calculations have been performed to obtain the lowest energy Li configurations at different concentrations. For a given Li concentration, Ti, Zr, and Hf based M_2CS_2 monolayers show lower binding energies (or stronger interaction) as compared to other S-functionalized MXenes. M_2CS_2 MXenes, where M= Ti, Hf, Zr, V,

and Nb, are capable of attracting at least a full layer of Li on both surfaces whereas other MXenes provide a positive voltage only at much lower Li concentrations. Importantly, Ti, V, and Nb based MXenes are capable of storing three layers of Li, which greatly enhances the storage capacity. Ti- and V-based M_2CS_2 MXenes provide relatively higher capacities, which are greater than 400 mAh/g, than that of other considered S-functionalized MXenes of this work and their O-terminated counterparts. Diffusion barriers for all the dynamically stable M_2CS_2 nanosheets are smaller than 0.22 eV, offering charging/discharging rates in battery applications.

Computational Methods

The density functional theory (DFT) calculations were performed using the Vienna *ab initio* simulation package (VASP).[17–20] A plane-wave energy cutoff was set to 500 eV. The electron-ion interactions were described by the projected augmented wave (PAW) method.[21,22] The generalized gradient approximation (GGA) based exchange-correlation potential was considered with the Perdew-Burke-Ernzerhof (PBE) pseudopotentials.[23,24] A vacuum space larger than 15 Å was used to avoid spurious interaction between monolayers. A Γ-centered 17×17×1 Monkhorst-Pack **k**-mesh was considered for primitive cell calculations. The number of k-points was scaled for the larger cell sizes. The supercell approach and the force-constant method were employed to calculate the phonon dispersion using PHONOPY code.[25] A 4×4×1 supercell structure with a k-points mesh of 4×4×1 was constructed to calculate the resulting forces on the perturbed atoms. We plotted phonon dispersion along the three high-symmetry points (Γ(0.0, 0.0, 0.0), M (1/2, 0.0, 0.0) and K (1/3, 1/3, 0.0)). The climbing image nudged elastic band (CI-NEB) method, as implemented in the VASP transition state tools, was applied to estimate the minimum energy diffusion paths.[26,27]

Results and Discussion

Stability of MXenes

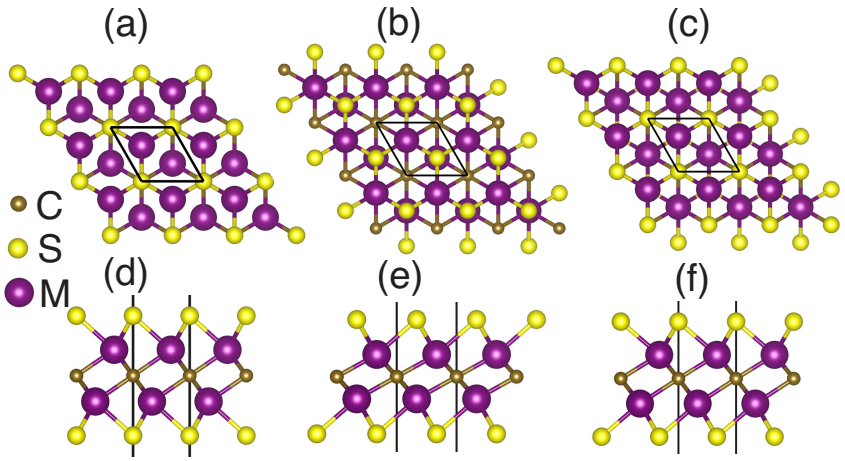

Figure 1: Top views of M_2CS_2 monolayers with (a) HCP, (b) FCC and (c)FCC-HCP surface structures, and the side views of (d) HCP, (e) FCC and (f) FCC-HCP surface structures

First, we considered different possible surface structures for M_2CS_2 (M= Sc, Ti, Zr, Hf, V, Nb, Ta, Cr, Mo, W) monolayers. The ground-state structure of bare-M_2C monolayers is hexagonal, where the C layer is sandwiched between the two M layers. Unterminated M_2S consists of three haxagonal atomic layers with ABC layer stacking with trigonal (D_{3d}) symmetry.[28] By changing the position of the S atoms on the surface, we predicted three different surface structures for sulfur atom, namely HCP, FCC, and HCP-FCC, as shown in Fig. 1. The HCP structure has the $P\bar{3}m1$ space group symmetry with both top and bottom S atoms residing directly above and below the same C atom. The FCC surface structure also possesses the $P\bar{3}m1$ symmetry. In the FCC structure, the top S atom is positioned directly above the bottom M atom, whereas the bottom S atom is at the right below the top M atom. The HCP-FCC structure has a mixed surface termination with the coexistence of HCP and FCC crystal configurations (see Fig. 1(c) and (f)). We also performed spin-unrestricted calculations to reveal whether the S-terminated MXenes develop any magnetism. While the unterminated MXenes may have a magnetic ground state depending on the transition metal atom, the S-terminated MXenes have nonmagnetic ground states. Besides, the adsorption

of Li ions on the MXene surfaces induces magnetism neither. To shed some light on the stability of sulfur surface termination, we studied the following reaction; $M_2C + 2S_{Bulk} \rightarrow M_2CS_2$, which represents the sulfuration of the unterminated MXene surface. Here, we calculated the formation energy of M_2CS_2 via E_{form}=E_{tot}[M_2CS_2]-2E_{tot}[Bulk S]-E_{tot}[M_2CS], where E_{tot}[M_2CS_2], E_{tot}[Bulk S] and E_{tot}[M_2C] are the calculated total energies of terminated MXene, bulk S and bare MXene, respectively. In this reaction, the source of S atom is bulk S with the P2/c space group, which composes of S_8 rings. The above reaction is found to be exothermic (i.e., $E_{form} < 0$), meaning that S-terminated MXene is stable against decomposition into S bulk and unterminated MXene sheet. Terminated MXene is 2-3 eV/S stable with respect to bare MXene depending on transition metal atom. This is expected since the surface termination groups stabilize the bare MXenes by saturating the dangling bonds.

The ground state structures of the materials are given in TABLE 1. M_2CS_2 with a 4B M element (Ti, Zr, and Hf) has the FCC structure as the minimum energy configuration, while that with a 6B M element has the HCP surface termination. Even though MXenes with Nb and Ta provide the lowest energy surface termination for FCC-HCP structures, the S atoms prefer to sit at the FCC sites in V related MXene. Our phonon calculations (Fig. 2) indicate that all those monolayers with the 4B, 5B, and 6B M atoms are dynamically stable. Even though Sc_2CO_2 is stable, our phonon calculations found that Sc_2CS_2 is dynamically unstable.

The computed lattice constants (a) and the M-S, M-C, and C-S bond lengths are summarized in TABLE 1. Our calculations are in good agreement with the values reported by previous research for Ti_2CS_2, V_2CS_2 and Mo_2CS_2.[4,13,29,30] The calculated lattice constants show that those values are larger than that of their O terminated counterparts (M_2CO_2). For instance, Ti, Zr, Hf, V, and Mo based M_2CO_2 have a values of 3.031, 3.309, 3.268,[31] 2.86,[32] and 2.99[33] Å, respectively . These values are more than 0.1 Å smaller than that of Ti, Zr, Hf, and V based S-terminated MXenes. We also found that M_2CS_2 MXenes have

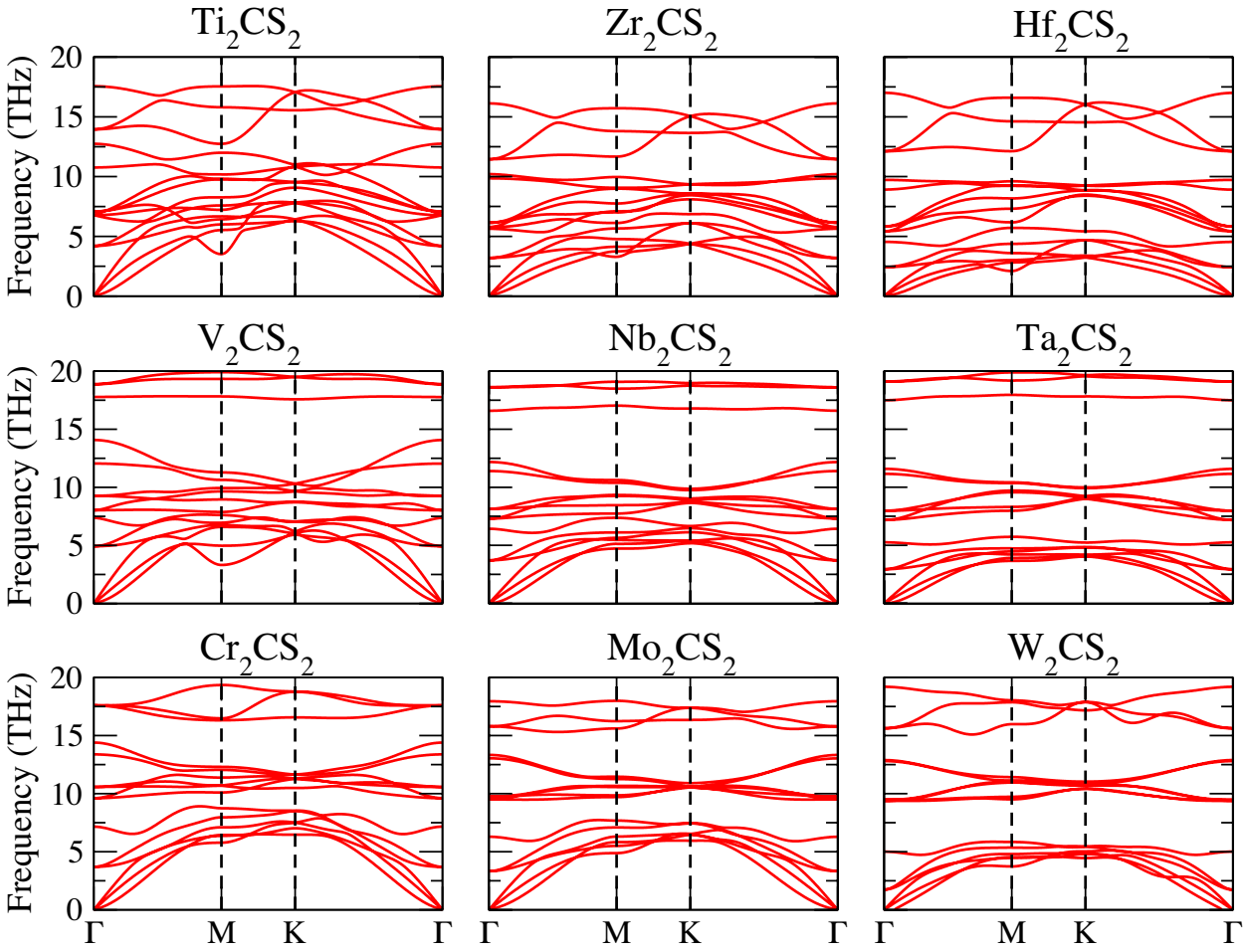

Figure 2: Phonon dispersion curves for stable S-functionalized MXenes

significantly longer M-S bond lengths than the M-O bond lengths of M_2CO_2 because the high electronegative O (3.5) which makes stronger and shorter bonds with M atoms compared to S, whose electronegativity is only 2.5. In addition, the S atom has a much larger radius than the O atom, which leads to a longer M-S bond as compared to the M-O bond. Such a large electronegativity difference between O and S also implies a larger charge on O, thereby larger O-Li attractive Coulomb interaction. M_2CS_2 with $3d$ transition metal atoms have the shortest bond lengths and lattice constants, as can be seen in TABLE 1. M-C and M-S bond lengths with $3d$ M atoms are shorter than that of $4d$ and $5d$ M atoms. These bond lengths in MXenes with $4d$ and $5d$ M atoms of the same column have approximately the same magnitude. This trend is correlated with the ionic radius (R) of the respective

Table 1: The ground state structures, lattice constants (a), M-S and M-C bond lengths, average Bader charge transfer (Δq) for each element in M_2CS_2. The data for Sc_2CS_2 material is not provided, since it is dynamically unstable. For Nb and Ta, two different C-S bonds exist due to their mixed HCP-FCC surface structures.

M	Ground State	a (Å)	M-S (Å)	M-C (Å)	C-S (Å)	Δq_C (e)	Δq_M (e)	Δq_S (e)
Ti	FCC	3.197	2.406	2.211	3.321	-1.843	1.739	-0.814
Zr	FCC	3.477	2.539	2.414	3.525	-1.925	1.915	-0.949
Hf	FCC	3.435	2.516	2.383	3.488	-2.160	2.125	-1.042
V	FCC	3.063	2.370	2.078	3.203	-1.703	1.504	-0.649
Nb	HCP-FCC	3.281	2.508	2.267	2.888 (3.393)	-1.823	1.672	-0.757
Ta	HCP-FCC	3.267	2.494	2.267	2.887 (3.357)	-2.061	1.914	-0.949
Cr	HCP	2.934	2.278	2.053	2.686	-1.353	1.188	-0.509
Mo	HCP	3.077	2.400	2.201	2.914	-1.410	1.280	-0.573
W	HCP	3.068	2.404	2.220	2.963	-1.574	1.438	-0.648

elements. For instance, $R_{Ti} = 60$ pm $< R_{Zr} = R_{Hf} \approx 86$ pm by assuming these three atoms are at +4 oxidization state.[34]

The Bader charge (Δq) on each atom are presented in TABLE 1. The Bader charge on the S atoms is at most 1e, which is significantly smaller than the Bader charge on O in O-based MXenes. The M and C atoms have opposite charge transfer with the approximately same magnitude. Thus, we can conclude that M-C bonds also have an ionic character. The amount of charge transfer increases when moving down in the periodic table as the electronegativity difference between M and C/S atoms rises. MXenes with $3d$ transition metals show lower Δq_C, Δq_M and Δq_S values than MXenes with $4d$ and $5d$ M atoms, indicating a weaker ionic bonding character in the former. The surface structure of MXenes considered in this work resembles (111) surface of bulk transition metal carbides and nitrides[35] which display a complex mixture of covalent/ionic/metal bonding character.[36] Therefore, one must be cautious in using Bader analysis to understand the bonding character and amount of charge transferred in such systems. Nevertheless, our Bader analysis predicted consistent results that allow us to qualitatively explain interaction strength of Li ions with MXenes and dependence of open circuit voltages on type of MXene.

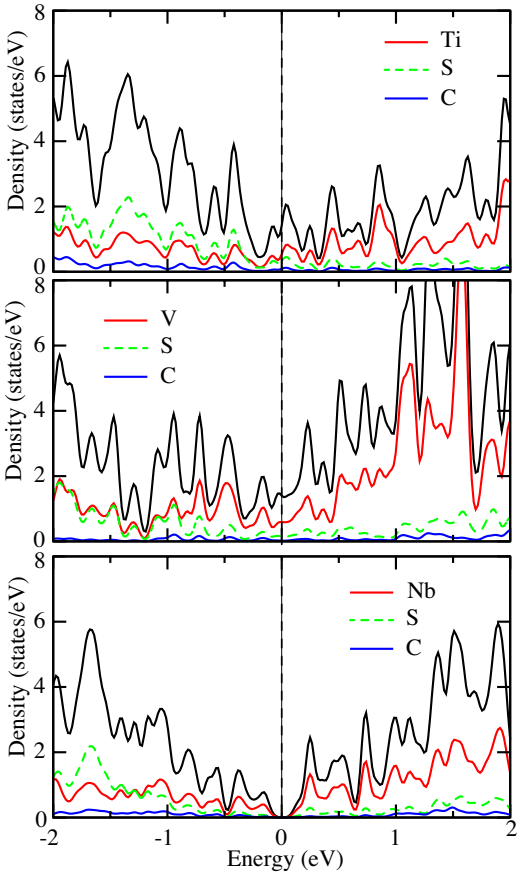

Figure 3: Density of state(DOS) of M_2CS_2, where M=Ti, V and Nb. The vertical dashed lines marks the Fermi level.

Electronic properties

Figure 3 shows the density of states (DOS) plots of selected MXenes, namely Ti_2CS_2, V_2CS_2 and Nb_2CS_2, due to their promise as electrode materials, as described in the next sections. Presence of metallic character with a good electronic conduction is a key factor for an excellent electrochemical performance of an electrode material. Ti_2CS_2 and V_2CS_2 exhibit metallic behavior with a significant DOS around the Fermi level, implying a good electrical conduction in these materials. However, Nb has a small band gap that is closed upon Li adsorption. Considering the electronic properties, Ti and V based MXene are expected to exhibit much better performance as compared to Nb-based MXene.

Table 2: The binding energy of a single Li (E_b) at different sites and Bader charge transfer (Δq) for each element when a single Li is adsorbed at the minimum energy site.

M	Ground State	E_b (eV/atom)				Δq_C (e)	Δq_M (e)	Δq_S (e)	Δq_{Li} (e)	Li-S (Å)
		Site A	Site B	Site C	Site D					
Ti	FCC	-2.226	-2.262	-	-	-1.852	1.736	-0.838	0.990	2.368
Zr	FCC	-2.462	-2.380	-	-	-1.933	1.924	-0.985	0.996	2.352
Hf	FCC	-2.300	-2.241	-	-	-2.154	2.127	-1.078	0.995	2.349
V	FCC	-1.348	-1.467	-	-	-1.719	1.510	-0.678	0.991	2.351
Nb	HCP-FCC	-1.549	-1.645	-1.248	-1.324	-1.822	1.682	-0.798	0.993	2.380
Ta	HCP-FCC	-1.201	-1.310	-0.920	-1.004	-2.055	1.885	-0.885	0.991	2.376
Cr	HCP	-1.428	-1.556	-	-	-1.357	1.203	-0.553	0.991	2.367
Mo	HCP	-1.066	-1.209	-	-	-1.401	1.280	-0.607	0.991	2.358
W	HCP	-0.955	-1.113	-	-	-1.587	1.451	-0.686	0.991	2.352

Single Ion Adsorption

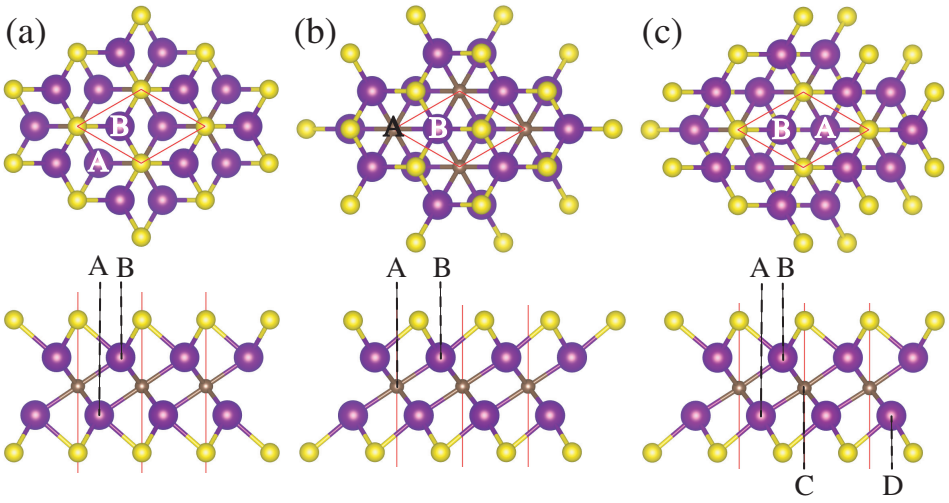

Figure 4: The possible Li adsorption sites for (a) HCC, (b) FCC and (c) HCP-FCC surface structures of M_2CS_2 MXenes.

Next, we investigated single Li adsorption on S-terminated MXenes using a 4×4 M_2CS_2 supercell. We identified the different adsorption sites for the different lattice structures, as shown in Fig. 4. Figure 4(a) shows the two possible sites on the HCP structure. While Li is directly above a bottom M atom in Site A, it resides above a M atom in Site B. Figure 4(b) denotes the possible adsorption sites on the FCC surface structure. Site A indicates a site on the surface right above a C atom, while Site B is directly above a M atom. Due to the reduced symmetry, we found four distinct adsorption sites for the mixed HCP-FCC surface structure

(Fig. 4(c)). Here, Site A and Site B are identified on the surface with HCP termination, whereas Site C and Site D are on FCC terminated surface. Site A and Site B are equivalent to Site A and Site B of the HCP surface structure, and the Site C and Site D are identical to the Site A and Site B of FCC surface structure.

The binding energy (E_{b}) per Li-ion was calculated as follows

$$E_b = \frac{1}{n}[E(\mathrm{M_2CS_2} + n\mathrm{Li}) - E(\mathrm{M_2CS_2}) - nE(\mathrm{Li})] \quad (1)$$

where $E(\mathrm{M_2CS_2}+x\mathrm{Li})$ is the total energy of MXene with Li, $E(\mathrm{M_2CS_2})$ is the total energy of bare MXene, $E(\mathrm{Li})$ is the energy of the Li atom obtained from body-centered-cubic (BCC) bulk crystal structure, and n is the number of adsorbed Li atoms in our computational unit cell. The calculated E_{b} values are given in TABLE 2. It is clear that the Li ions adsorbed on MXenes with group 4B M atom have the lowest E_{b} energy which increases when M changes from group 4B to 6B. The above observation indicates that the strongest Li-S bonding exists in the MXenes made of group 4B transition metal atoms. $\mathrm{Zr_2CS_2}$ shows the lowest E_{b} that is -2.462 eV, while the highest E_{b} is calculated for $\mathrm{W_2CS_2}$.

Regarding the adsorption site, the Li atom prefers to bind to the Site B on $\mathrm{M_2CS_2}$, where M= Ti, V, Nb, Ta, Cr, Mo and W. However, the Site A is energetically more favorable for $\mathrm{Zr_2CS_2}$ and $\mathrm{Hf_2CS_2}$. One reason for this different behavior of $\mathrm{Zr_2CS_2}$ and $\mathrm{Hf_2CS_2}$ monolayers is attributed to their much larger lattice constants.

The Bader charge transfer calculations in TABLE 2 show that Δq_{Li} ($\sim 1e$) is almost the same for all $\mathrm{M_2CS_2}$ MXenes. The charge on the S atoms plays a crucial role in determining the binding energy of Li. For instance, for $\mathrm{W_2CS_2}$, the Bader charge on S atoms is only $0.648e$, which is significantly smaller than that on S atoms of $\mathrm{M_2CS_2}$ with M=Ti, Zr and Hf. Therefore, the Li-S attractive interaction is stronger in the latter system. The larger the charge on S, the stronger the interaction with Li.

In our calculations, we did not include van der Waals (vdW) interaction. In our systems, binding energies of Li atoms on the MXene surfaces are much higher than the typical energies

found for vdW interaction. To show this, we performed test calculations by including vdW corrections. Binding energy of a single Li atom on a 4×4 surface cell of Ti_2CS_2 is -2.262 eV without vdW. This energy becomes -2.200 eV, when we include vdW interaction using DFT-D3 formalism.[37] The difference between these two binding energies is 0.062 eV, which is very small as compared to the computed binding energies in our systems.

Multiple Ion Adsorption

Before calculating the voltage, we searched out the most stable Li configurations for different intermediate Li concentrations on S-functionalized MXenes using cluster-expansion (CE). In most of the previously published computational battery papers, the possible adsorption configurations for ions have been found by checking a few numbers of possible adsorption structures for each concentration. This can cause substantial errors in the calculation of voltage at intermediate Li concentrations and the prediction of storage capacity. For instance, in recent work on Li adsorption on Mo_2CS_2 monolayer, the calculated theoretical specific capacity was found to be 410 mAh/g.[30] However, our capacity calculations based on CE predicts a much lower capacity of 49.4 mAh/g. Therefore, to predict the storage capacity and voltage correctly, the CE method was chosen in our work. In the CE method, for a given configuration, the formation energy (E_f) of $Li_xM_2CS_2$ with respect to M_2CS_2 and $Li_2M_2CS_2$ is defined as

$$E_f = E_{tot}[Li_{2-2x}M_2CS_2] - E_{tot}[M_2CS_2] - (1-x)E_{tot}[Li_2M_2CS_2] \quad (2)$$

Here, x is the fraction of Li atoms out of the total number of Li atoms in a fully loaded MXene. In other words, x=1 denotes the adsorption of two layers of Li (one Li layer on each surface). $E_{tot}[Li_xM_2CS_2]$, $E_{tot}[Li_2M_2CS_2]$, and $E_{tot}[M_2CS_2]$ are the calculated formula unit energies of $Li_xM_2CS_2$ $Li_2M_2CS_2$, and M_2CS_2 monolayers, respectively. We computed the total energy of at least 150 configurations with different Li concentrations for each M (i.e., transition metal atom). Then, we constructed the CE Hamiltonian of $Li_xM_2CS_2$ by fitting

to the first-principles energies. The formation energies allow us to construct the ground state energy vs. composition curve (called convex hull), which consists of lines connecting all the lowest energy structures that are most likely to form in experiments. Convex hull identifies thermodynamically stable structures at T = 0 K, which can be considered as free energy without the inclusion of the entropy term. The cross-validation score, providing the predictive power of the cluster expansion, of the CE fitting for different MXenes are less than 10 meV, which depicts that our CE Hamiltonian is accurate enough to predict the formation energies of $Li_xM_2CS_2$ as a function of Li concentration. Figure 5 denotes the calculated formation energies as a function of Li concentration obtained from the cluster expansion calculations using the ATAT code.[38–40] We found several stable Li configurations at intermediate concentrations. The shape of the convex hull is similar for the transition metal elements in the same column of the periodic table. MXenes with group 4B and 5B elements have a minimum in the convex hull at a lower concentration than the group 6B elements, allowing more structures to exist on the convex hull. Cr-based MXene has no structure on the convex hull when the Li concentration is larger than x =0.34 due to its small lattice constant, resulting in enhanced repulsive interaction between Li ions with increasing Li concentration, and thereby pushing the structures away from the convex hull. MXenes with group 4B elements have lower minimum formation energies than that with group 5B and 6B elements. Figure 6 shows the structure of minimum energy intermediate configurations extracted from the convex hull plots. In the present study, we neglected the temperature effects. Some of the ion orderings that are within a small energy window above the convex hull may become accessible at finite temperatures. By considering the typical operation temperatures of batteries, we can predict the accessible structures from the convex hull plots. For instance, MXenes with group 4B and 5B elements have configurations very close to the convex hull, which can be accessible with increasing temperature.

We also calculated the Li adsorption on $Li_2M_2CS_2$, where M_2CS_2 already has two layers of Li adsorbed (one Li layer on each surface). Figure 7 shows the formation energy for

$Li_{2+x}M_2CS_2$, where M=Ti, V and Nb. Further addition of Li ions to $Li_2M_2CS_2$ makes the formation energy positive, meaning that further Li adsorption is not energetically possible at T= 0K. At $x = 0.5$ (or one more Li layer), the formation energy is slightly positive. At finite temperatures, the structures with slightly positive energies may be accessible as entropy term lowers the formation energy. Therefore, it is possible to store three layers of Li on these three MXenes.

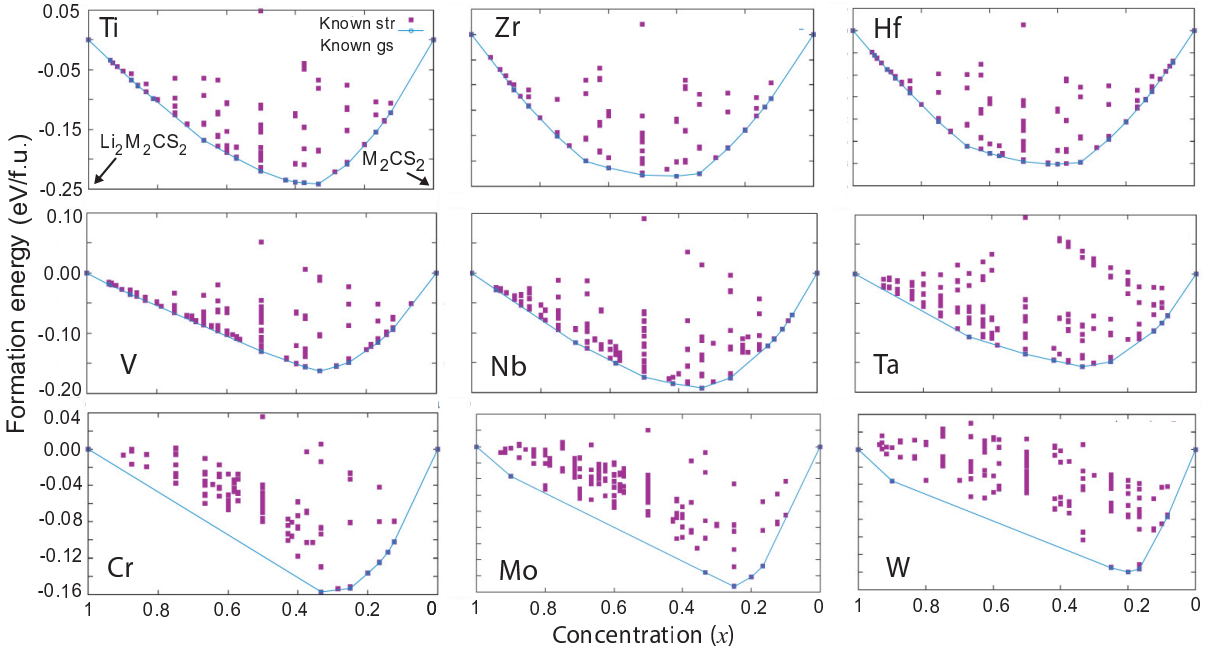

Figure 5: Calculated formation energies of $Li_xM_2CS_2$. The blue line in each figure indicates the convex hull. The configurations marked with blue empty squares are those that are the thermodynamically stable (at T = 0 K) ordered configurations of lithium ions and vacancies on S-functionalized MXenes.

We studied the change in lattice constant (Δa) when both surfaces are covered with Li atoms, based on the expression $\Delta a = \frac{(a-a_0)\times 100}{a_0}$ as shown in TABLE 4. Here, a_0 is the lattice constant of bare MXene, while a is the lattice constant of $M_2CS_2Li_2$. All materials show surface expansion when Li atoms are attached to the surfaces. 3*d*-transition metal atom-based M_2CS_2 exhibit high in-plane lattice parameter expansion in line with strong interactions with Li observed for these monolayers. $V_2CS_2Li_2$ possesses the highest increase which is around 5.8%. 5*d*-transition metal-based M_2CS_2 MXenes show the lowest change,

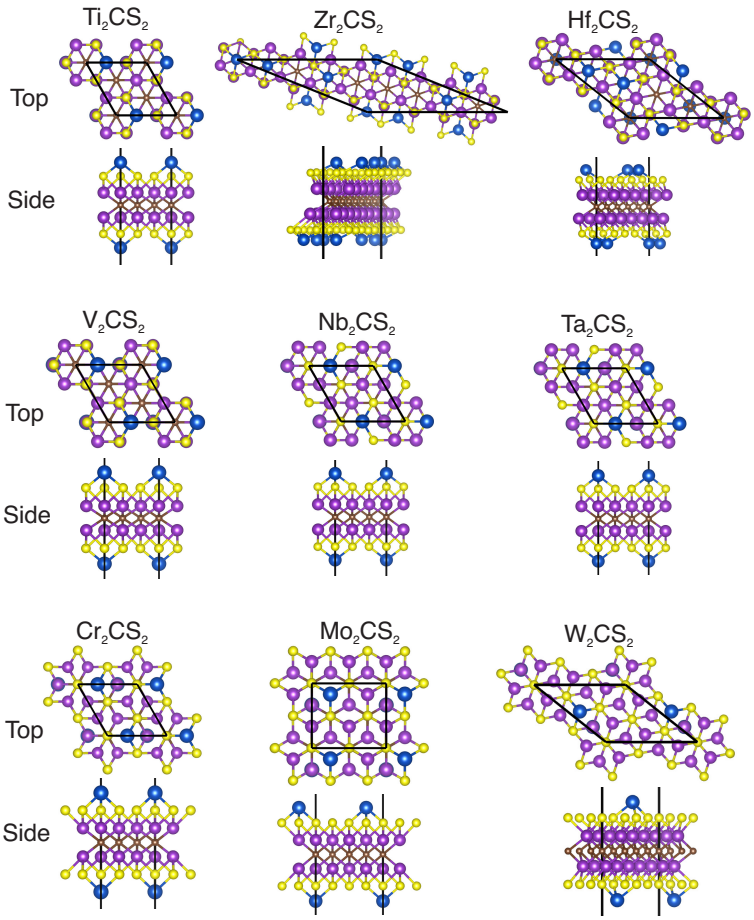

Figure 6: Top and side views of lowest energy multiple ions adsorbed M_2CS_2 MXenes structures obtained from the minimum of convex hull.

which is only 1.4%.

Figure 8 denotes the E_b as a function of Li content. Here, the Li content is 2 when all lowest energy adsorption sites on both surfaces are occupied. The common feature of the results for all MXenes is that the binding energy rises (approaching the positive side) while the Li content increases. It is clear that E_b of M_2CS_2 MXenes with M elements in the same column of the periodic table exhibit similar behavior with changing Li content. For a given content, the lowest (more negative) E_b can be found for the 4B column, while the highest values can be obtained for the 6B column. Thus, Li adsorption on Ti_2CS_2, Zr_2CS_2, and Hf_2CS_2 are more stable, and it will be useful for avoiding the formation of bulk Li (or Li clusters) during the charging/discharging processes. W_2CS_2 has positive E_b after a 1.5 Li

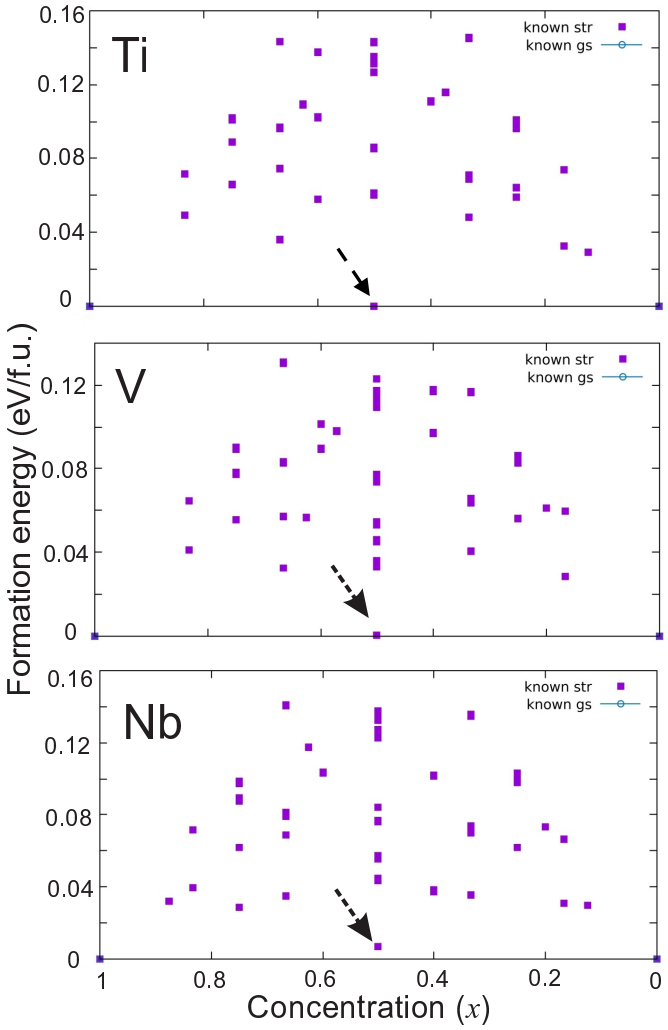

Figure 7: Calculated formation energies of $Li_{2+x}M_2CS_2$ as a function of Li concentration. Arrows show the minimum energy structures at x=0.5.

content, implying that the adsorption of two layers of Li (one Li layer on each surface) is not energetically favorable.

TABLE 3 summarizes the variation of M-S and S-Li bond lengths as a function of Li content. Adsorption of a single Li ion on a 4×4 cell does not significantly modify the M-S bond lengths adjacent to adsorbed Li ion. For full Li coverage, M-S bond lengths are elongated by about 2-7% depending on MXene. Li-S bond lengths decrease (increase) as Li content increases for Ti_2CS_2, Zr_2CS_2, Hf_2CS_2, Nb_2CS_2, Ta_2CS_2 and V_2CS_2 (Cr_2CS_2, Mo_2CS_2 and W_2CS_2). Variation of M-S and Li-S bond lengths in Zr_2CS_2 and Hf_2CS_2 suggest that Li ions interact with S atoms and move closer the MXene sheet due to the large lattice

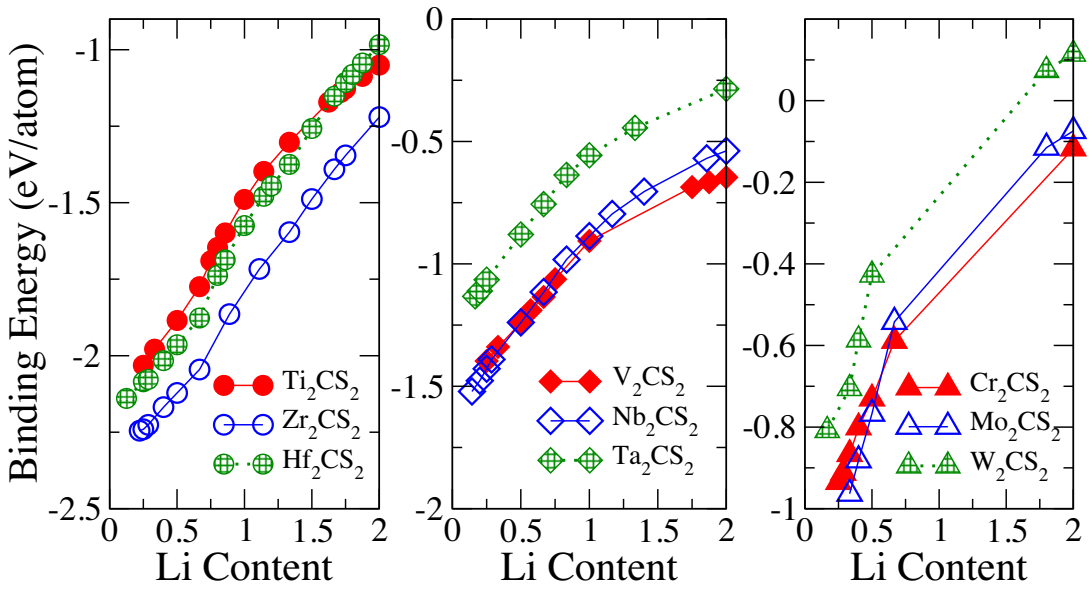

Figure 8: Binding energy (E_b) as a function of Li content.

Table 3: Variation of M-S and Li-S bond lengths, and lattice parameter a as a function of Li content.

Monolayer	a(Å) No Li	M-S No Li	Li-S Single Li	M-S Single Li	a(Å) Full coverage	Li-S Full coverage	M-S Full coverage
Cr_2CS_2	2.934	2.280	2.367	2.267-2.289	3.042	2.391	2.412
Mo_2CS_2	3.077	2.400	2.358	2.392-2.419	3.139	2.402	2.451
W_2CS_2	3.068	2.404	2.352	2.396-2.424	3.113	2.478	2.454
Ti_2CS_2	3.197	2.406	2.370	2.420-2.446	3.270	2.293	2.518
Zr_2CS_2	3.477	2.540	2.352	2.592	3.550	2.240	2.717
Hf_2CS_2	3.435	2.516	2.349	2.564	3.495	2.270	2.669
Nb_2CS_2	3.281	2.508	2.370	2.533	3.344	2.309	2.643
Ta_2CS_2	3.267	2.494	2.375	2.502-2.528	3.316	2.338	2.618
V_2CS_2	3.063	2.371	2.351	2.355-2.413	3.242	2.293	2.464

constants in these MXenes (TABLE 1) and Li adsorption site (Site A) that have enough space to accommodate Li ion closer to MXene.

Ab initio molecular dynamics (MD) simulations were performed to check thermal stabilities of sulfur-functionalized MXenes, as denoted in Fig. 9. We performed MD simulations within an isothermal-isobaric (NPT) ensemble for 4×4 supercell structures of Ti, V and Nb based-MXenes with full coverage of Li.[41,42] We selected 400 K temperature to see whether thermally induced perturbations will induce any structural transformation or distortion and Li release. The variations on the temperature and the total energy are commensurate to

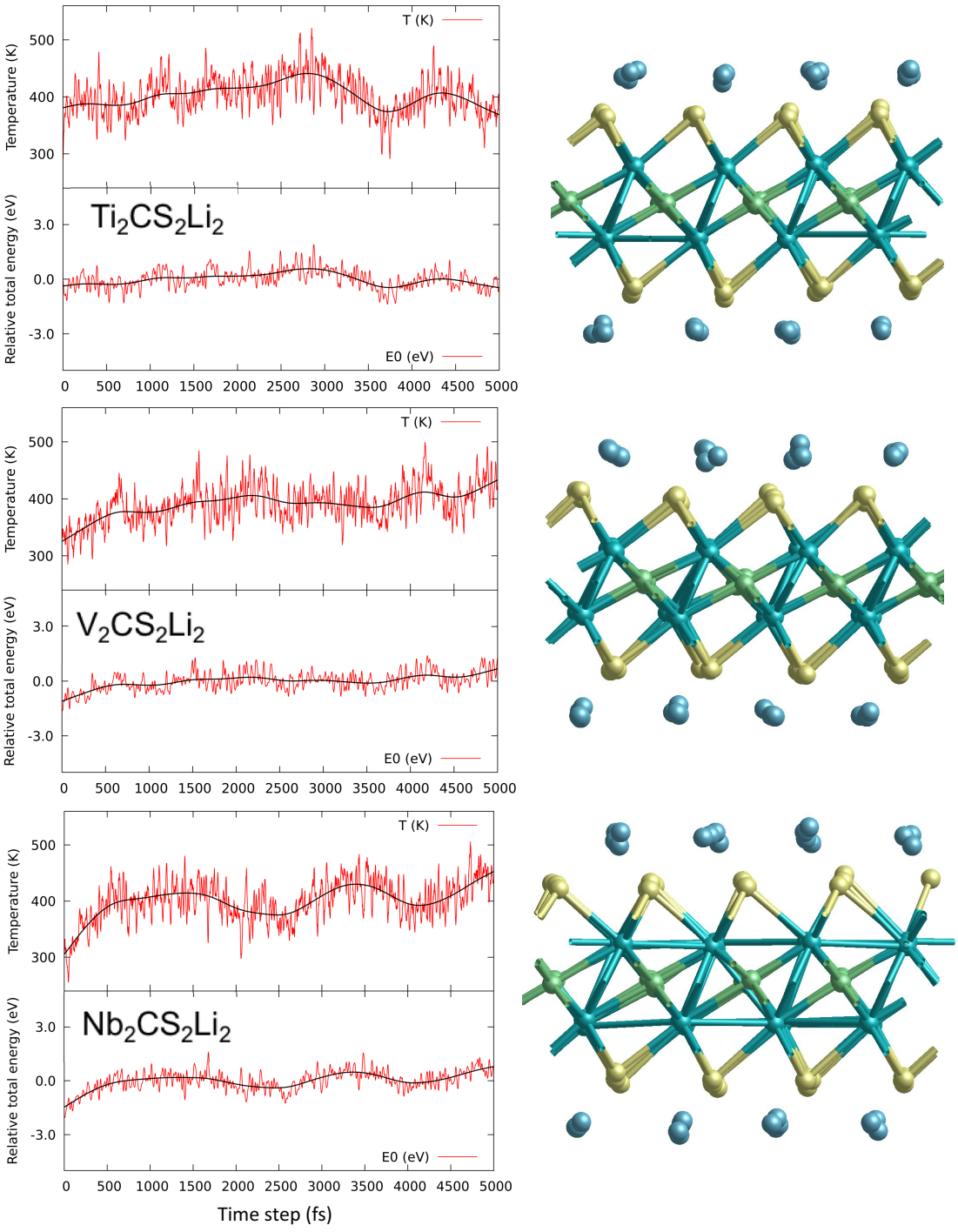

Figure 9: Ab initio molecular dynamics simulations for Ti, V and Nb based MXenes with full coverage of Li at 400 K. Variation of temperature and energy is plotted as a function of time. The snapshot of final structure after 5 ps is also included for each system.

Table 4: The in-plane lattice constant change (Δa), maximum voltage (V_{max}), average voltage (V_{avg}), gravimetric capacity (C_g) and diffusion barrier (E_{diff}). Here, V_{avg1} was calculated using Eq. 4 for positive voltage ranges, while V_{avg2} was computed employing $\sum_i^N V_i/N$ where i is the step number and N is the number of steps in Fig. 10.

M	Δa(%)	V_{max} (V)	V_{avg1} (V)	V_{avg2} (V)	C_g (mAh/g)	E_{diff} (eV)
Ti	3.6	2.031	1.050	0.997	288.6	0.176
Zr	2.1	2.245	1.220	1.362	196.8	0.218
Hf	1.7	2.140	0.983	0.988	120.0	0.206
V	5.8	1.397	0.646	0.730	279.4	0.199
Nb	1.9	1.521	0.538	0.724	194.4	0.211
Ta	1.5	1.133	0.444	0.564	79.9	0.210
Cr	3.7	0.935	0.589	0.561	96.8	0.177
Mo	2.0	0.963	0.767	0.582	49.4	0.210
W	1.4	0.808	0.705	0.705	20.0	0.217

each other. Furthermore, our simulations revealed no structural transformation for any of the considered systems during 5 ps. We did not observe the formation of Li_xS that can result in capacity fading. In summary, all three systems are found to be thermally stable at temperatures higher than the operating temperatures of batteries.

Electrochemical Properties

We next studied the electrochemical properties of the S-fuctionalized MXenes. The chemical reaction for adsorbing Li on $M_2CS_2Li_{x1}$ and forming $M_2CS_2Li_{x2}$ can simply be described using Eq. 3, where x_1 and x_2 are the Li content before and after the reaction.

$$(x_2{-}x_1)Li^+ + (x_2{-}x_1)e^- + M_2CS_2Li_{x1} \longleftrightarrow M_2CS_2Li_{x2} \quad (3)$$

The open-circuit voltage (OCV) for the above chemical reaction can be predicted using the Gibbs free energy ($G(x)$), which can be written as $G(x) = \Delta E + P\Delta V - T\Delta S$. Here, ΔE is internal energy change (obtained from our DFT calculations at T= 0K), P indicates pressure, ΔV is volume change, T is temperature, and ΔS is entropy change. However, $P\Delta V \approx 10^{-5}$ eV and $T\Delta S \approx 25$ meV. By neglecting these two terms, we are able to

approximate the average voltage (V) by only determining ΔE as follows.

$$V \approx \frac{E[\mathrm{M_2CS_2Li_{x1}}] - E[\mathrm{M_2CS_2Li_{x2}}] + (x_2 - x_1)E[\mathrm{Li}]}{(x_2 - x_1)e} \tag{4}$$

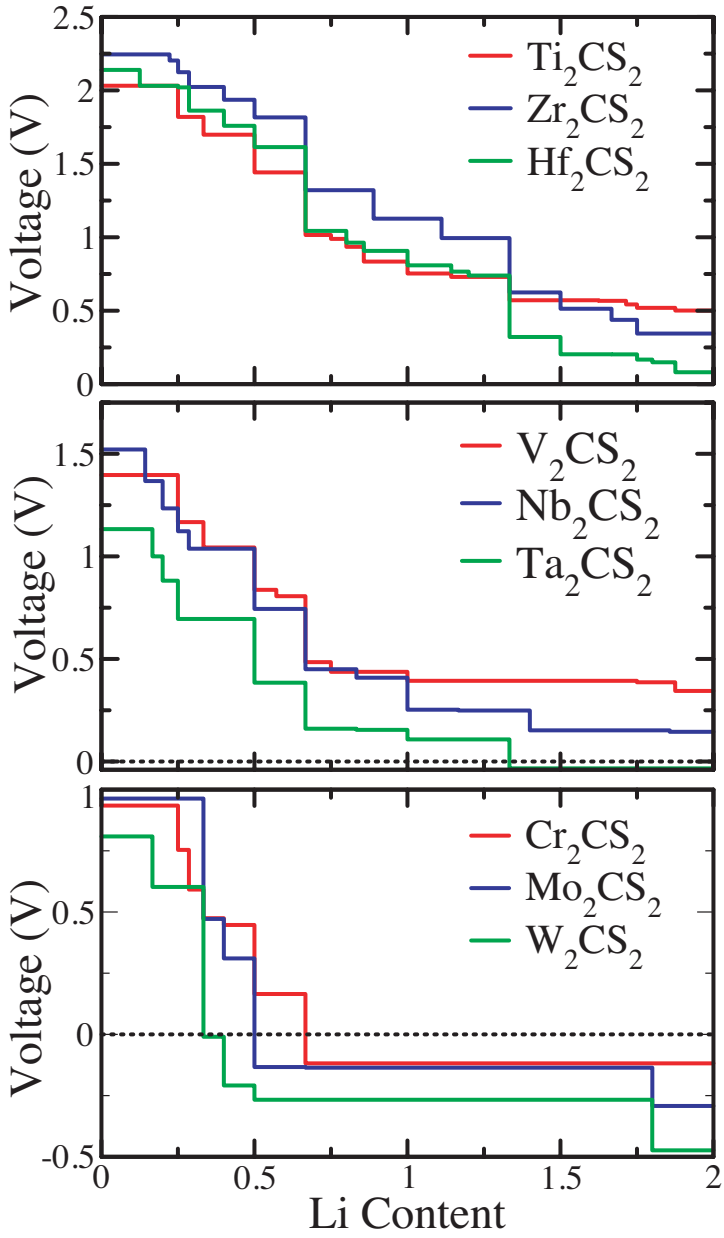

Figure 10: Calculated voltage as a function of Li Content.

Using Eq. 4, we calculated the open-circuit voltage as a function of Li concentration, as shown in Fig. 10. When calculating the voltages, we considered the structures on the

convex hull (Fig. 5). Usually, the V and Mo containing MXenes with O or mixed O/OH terminations have higher OCV and can be cycled to higher potentials vs. Li/Li^+ compared to Ti containing MXenes. However, here, we found that the highest maximum voltages were obtained for sulfur functionalized MXenes with M atom from group 4B of the periodic table (i.e., Ti, Zr, and Hf). The explanation for the discrepancy in our calculations and the previous experimental/theoretical results is that sulfur functionalized MXenes with Ti, Zr, and Hf exhibit the strongest binding energies for Li as a result of larger negative charge on S atoms, giving rise to strong attractive interaction with positively charged Li-ions. For instance, the Bader charge on the S atom is more than $0.84e$ for Ti, Zr, and Hf, whereas it is less than $0.7e$ for both V and Mo. The charge on Li-ion is almost the same for all consider systems. Since the value of voltage is substantially dependent on the strength of binding between the host material and Li-ion, the highest maximum voltages were obtained for Ti, Zr, and Hf containing sulfur functionalized MXenes. The maximum voltages for Ti, Zr, and Hf are larger than 2 V. M_2CS_2 with M element from group 5B provides the next highest maximum voltages, which are greater than 1 V. The lowest voltage for a given Li content is obtained from M_2CS_2 monolayers with M atoms from group 6B, where voltages are always less than 1 V. It is clear from Fig. 10 that voltages computed for M_2CS_2 with Ti, Zr, Hf, V, and Nb do cross zero even when the Li content is approaching 2. However, the voltage of Ta_2CS_2 becomes negative at around 1.33 Li content, which indicates that two layers of Li cannot be stored using Ta_2CS_2 monolayer. The computed voltage for Cr_2CS_2, Mo_2CS_2 and W_2CS_2 become negative for low Li contents, designating that very low capacities can be expected from these MXenes. TABLE 4 summarizes the maximum voltage (V_{max}) and average voltage (V_{avg}) for each M_2CS_2 monolayer. The theoretically calculated V_{max} for bare Ti_2C is around 0.6 V and that for Ti_2CO_2 is 1.94 V.[43] Ti_2CS_2 provides approximately the same V_{max} (2.03 eV) as it's O-functionalized counterpart. Bare Mo_2C monolayers possesses V_{max} of 0.95 V[44] which is almost equal to V_{max} of Mo_2CS_2 .

The theoretical maximum gravimetric capacity (C_g) of M_2CS_2 MXenes can be obtain

from

$$C_g = \frac{x_{\max} \times z \times F \times 10^3}{M_{\mathrm{M_2CS_2}} + x_{\max}\mathrm{Li}} \tag{5}$$

where $x_{\max}$ is the maximum Li content before the voltage of the system become negative, z is the valency of ion ($z = 1$ for Li), F is the Faraday constant (26.81 Ah/mol), and $M_{\mathrm{M_2CS_2+x_{max}Li}}$ is the total atomic mass of the system with $x_{\max}$ of Li. Note that we also included the mass of adsorbed Li atoms, which is usually neglected when calculating the capacity. This causes the overestimation of the storage capacity.

From TABLE 4, we notice that the highest C_g (288.6 mAh/g) can be obtained for Ti_2CS_2 due to its low total atomic weight and the ability to adsorb full Li layers on both surfaces. Next lightest M_2CS_2 MXene is V_2CS_2 and it also possesses a high capacity (279.4 mAh/g). Even though Cr_2CS_2 is the third lightest MXene in TABLE 4, it exhibits very low capacity due to small $x_{\max}$. Despite the fact that two full layers of Li can be stored on Zr, Hf, and Nb based M_2CS_2, they provide low capacity compared to Ti_2CS_2 and V_2CS_2 due to their high total atomic masses. The theoretical C_g of Ti_2CO_2 was reported as 350 mAh/g.[45] The theoretical values calculated for O-terminated V_2C and Nb_2C are 335 and 250 mAh/g, respectively. O-based MXenes possess higher theoretical values than S-based MXenes as a consequence of having a low atomic mass for O termination. The theoretical capacity calculated for bare Ti_2C and Ti_3C_2 are 440 and 320 mAh/g, respectively. Even though these are much higher than that of S-functionalized Ti_2C, they have very low open-circuit voltages, which are 0.44 V for Ti_2C and 0.62 V for Ti_3C_2.[45–47] The theoretically and experimentally obtained capacity for graphite is around 372 mAh/g, but its open-circuit voltage is very low (0.2 V).[47,48] Ti_2NS_2 and V_2NS_2 nitride MXenes have capacities around 300 mAh/g with average open-circuit voltages 0.64 V and 0.82 V, respectively.[49] Whereas Ti_2CS_2 provides a capacity close to 288 mAh/g with an average open-circuit voltage of 1.050 V.

In our previous analysis, we computed C_g by considering two Li per formula unit or two Li layers (one layer on each surface of monolayer). However, our cluster expansion

calculations revealed that Ti_2CS_2, V_2CS_2 and Nb_2CS_2 may store up to three Li per formula unit (or three layers of Li), giving rise a significant storage enhancement. Then, the storage capacities become 417.4 mAh/g for Ti, 404.5 mAh/g for V, and 284.4 mAh/g for Nb. Since we did not include entropy term, the voltage becomes negative ($\sim$−0.1 V) when increasing the number of adsorbed Li layers from two to three. Inclusion of this term may stabilize the multilayer adsorption on each surface of MXene monolayer. Therefore, our calculations propose that S-functionalized Ti_2CS_2, V_2CS_2 and Nb_2CS_2 are likely to have storage capacities larger than O-terminated Ti_2CO_2, V_2CO_2 and Nb_2CO_2.

Diffusion Barrier

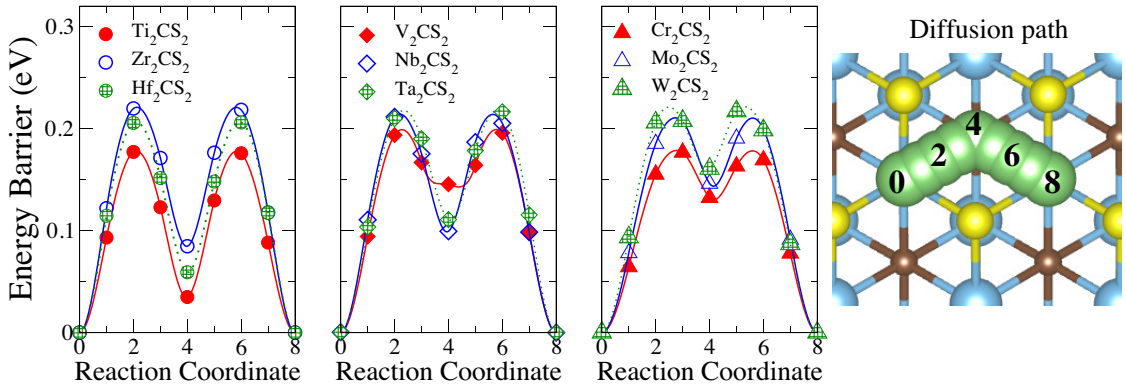

Figure 11: Diffusion energy barrier profiles for a single Li adsorbed on a 4×4 M_2CS_2 supercell. The most right structure denotes the typical diffusion path for the Li ion. Numbers label the image number along the diffusion path. "0" and "8" are the initial and final positions, respectively. Initial path was a straight line between initial and final points, which relaxes into a kind of "v" shape path. Image 4 is the local minima along the path which corresponds to the Site A in Fig. 4(b).

A low diffusion barrier is an essential property of an electrode to achieve high kinetics of metal ions. The high mobility of Li ions leads to good charging and discharging rates and high power densities in batteries. In order to study the ion kinetics, we performed CI-NEB calculations for single ion adsorbed systems. The computed energy barriers as a function of reaction coordinates are shown in Fig. 11, and maximum energy barriers are mentioned in TABLE 4. The energy barrier is lower for 3*d*-transition metal-related M_2CS_2 MXenes than

others. This can be due to the lower charge transfer of S atoms of Ti, V, and Cr atoms compared to the members of respective columns in the periodic table. Thus, Li-S attraction is low in respective MXenes. The lowest energy barrier was obtained for Ti_2CS_2, which is 0.176 eV. The next smallest energy barrier is for V_2CS_2, which is 0.199 eV. It is reported that single Li adsorbed on a 4×4 supercell of V_2C provides very small diffusion barrier (0.02 eV) while that of V_2CO_2 posses 0.24 eV.[4] The higher barrier in O-based MXene is due to the larger interaction between Li and O than that between Li and S. These trends were also observed for Zr based MXenes where Zr_2C has a negligible energy barrier, and Zr_2CO_2 has a barrier approximately 0.5 eV,[50] while Zr_2CS_2 has a barrier of only 0.218 eV. The calculated diffusion barriers of M_2CS_2 are much lower than that of commercial graphite (0.45-1.2 eV).[30,51] Moreover, the calculated diffusion barriers for M_2CS_2 are smaller than the energy barrier for Li diffusion in TiO_2 with a barrier of 0.60 eV[52] and high-capacity bulk silicon anode materials with a diffusion barrier around 0.57 eV. To check the effect of zero-point energy (ZPE) on the diffusion barriers, the diffusion process for a single Li ion on the surface of Ti_2CS_2 (which has the lowest diffusion barrier energy) was checked. The result shows that the ZPE term reduces the barrier energy by at most 0.01 eV, and the diffusion barrier becomes 0.166 eV (from 0.176) when including the ZPE term. So, we can conclude that the effect of ZPE is small as compared to the calculated diffusion barrier values.

Figure 12 denotes the diffusion barrier for a Li ion which is surrounded by other Li ions. As expected, the presence of adjacent Li ions strongly modifies the values and diffusion profiles due to the repulsive interaction among the positively charged Li ions. In these calculations, we only considered Ti_2CS_2, V_2CS_2 and Nb_2CS_2 due to their potential. We calculated the diffusion paths and energy barriers for a Li ion on a $4\times4\times1$ supercell, where only a single adsorption site is empty to facilitate the migration of adjacent Li ions into this empty site. Our calculations found that energy barrier increases to 0.41, 0.48 and 0.43 eV for Ti_2CS_2, V_2CS_2 and Nb_2CS_2, respectively. Regardless of Li concentration, these MXenes are expected to offer faster kinetics for the battery operations as compared to commercial

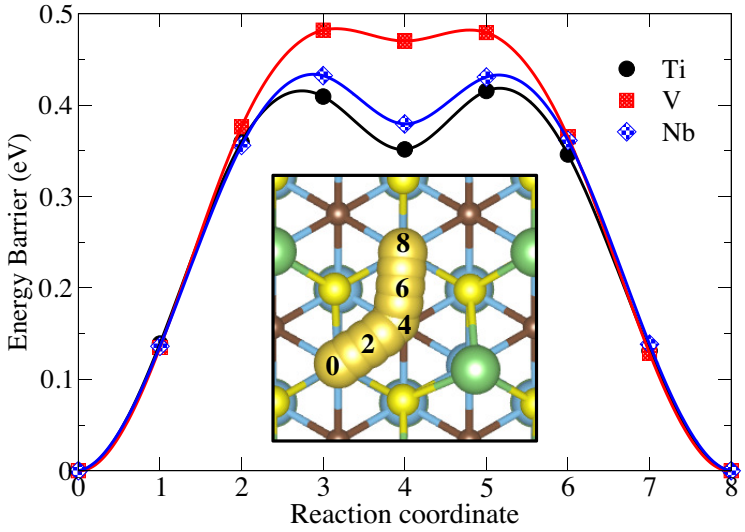

Figure 12: Diffusion energy barrier profiles for a single Li on M_2CS_2 (M=Ti, V and Nb) for high Li concentration. Inset shows the typical diffusion barrier of the Li ion on MXene surface with full coverage. Moving Li ion is depicted with yellow color. Numbers label the image number (or the position of Li atom) along the diffusion path. "0" and "8" are the initial and final positions, respectively. Initial path was a straight line between initial and final points, which relaxes into the path shown in the inset.

electrodes and computational predicted systems listed above.

Among the 2D materials, graphite is the most widely used anode material for Li-ion batteries with a theoretical capacity of about 372 mAh/g. Transition metal dichalcogenides (TMDCs) exhibit high initial capacities (1290 mAh/g). However, they suffer from poor cycling performance as a result of a phase transition (from 1H-MoS_2 to 1T-MoS_2) mediated conversion reaction in the first discharge cycle, leading to poor capacity retention.[53,54] Moreover, while some TMDCs have high electronic conductivity, many of them are semiconducting.[55,56] While transition metal oxides exhibit high redox activity in intercalation reactions with a high working potential, low electronic conductivity of oxides should be improved by mixing them with a conductive additive to improve their performance.[57] Considering the above-mentioned arguments, sulfur-functionalized MXenes promise a good capacity that can be improved by building heterestructures.[58] Importantly, predicted systems offer a high-rate charging capability that is one of the key factors pursued in battery research.

Conclusion

In summary, we conducted a density functional theory-based study of the structural, stability, electrochemical, and ion kinetics of sulfur functionalized M_2CS_2 MXenes, where M= Sc, Ti, Zr, Hf, V, Nb, Ta, Cr, Mo, and W. First, we identified the lowest energy S absorption site on bare M_2C MXenes. Depending on the type of M element, the S atom prefers to site at different sites. From our phonon calculations at T = 0K, we confirmed that all M_2CS_2 MXenes, except Sc_2CS_2, are dynamically stable. M_2CS_2 with M = Ti, Zr, Hf, V, and Nb MXenes can attract full Li coverage on both surfaces. Our cluster expansion calculations revealed the correct Li adsorption structures at different concentrations. We found that Ti_2CS_2, V_2CS_2 and Nb_2CS_2 promise to have gravimetric capacities higher than their O-terminated counterparts. Ti_2CS_2 and V_2CS_2 have low diffusion barriers, which are around 0.19 eV. As a result, Ti_2CS_2 and V_2CS_2 have better ion-storage and fast ion diffusion properties. Due to the strong monolayer-Li^+ interaction, M_2CS_2 monolayers with Ti, Zr and Hf have larger open-circuit voltages where the maximum of the voltages exceed 2 V, and the average voltages are around 1 V. By considering all the above facts, not only Ti_2CS_2 but also V_2CS_2 and Nb_2CS_2 appears as candidate materials for the energy storage applications due to high voltages, large capacities, low diffusion barriers and stabilities at high temperatures.

Acknowledgment

Computational resources were provided by the HPC infrastructure of the University of Antwerp (CalcUA), a division of the Flemish Supercomputer Center (VSC), which is funded by the Hercules Foundation. This work is supported, in part, by The Scientific and Technological Research Council of Turkey (TUBITAK) under contract number 118F512 and the Air Force Office of Scientific Research under award number FA9550-19-1-7048. This work was performed in part at the Center for Nanoscale Materials, a U.S. Department of Energy Office of Science User. The facility, and supported by the U.S. Department of Energy, Office

of Science, under contract no. DE-AC02-06CH11357.

References

1. Pomerantseva, E.; Gogotsi, Y. Two-dimensional heterostructures for energy storage. *Nature Energy* **2017**, *2*, 17089.

2. Sun, Y.; Chen, D.; Liang, Z. Two-Dimensional MXenes for Energy Storage and Conversion Applications. *Mater. Today Energy* **2017**, *5*, 22 – 36.

3. Anasori, B.; Lukatskaya, M. R.; Gogotsi, Y. 2D Metal Carbides and Nitrides (MXenes) for Energy Storage. *Nat. Rev. Mater.* **2017**, *2*, 16098.

4. Li, Y.-M.; Guo, Y.-L.; Jiao, Z.-Y. The effect of S-functionalized and vacancies on V_2C MXenes as anode materials for Na-ion and Li-ion batteries. *Current Applied Physics* **2020**, *20*, 310 – 319.

5. Aierken, Y.; Sevik, C.; Gülseren, O.; Peeters, F. M.; Çakır, D. MXenes/graphene heterostructures for Li battery applications: a first principles study. *J. Mater. Chem. A* **2018**, *6*, 2337–2345.

6. Wang, F.; Wang, Z.; Zhu, J.; Yang, H.; Chen, X.; Wang, L.; Yang, C. Facile synthesis SnO_2 nanoparticle-modified Ti_3C_2 MXene nanocomposites for enhanced lithium storage application. *Journal of Materials Science* **2017**, *52*, 3556–3565.

7. Feng, L.; Zha, X.-H.; Luo, K.; Huang, Q.; He, J.; Liu, Y.; Deng, W.; Du, S. Structures and Mechanical and Electronic Properties of the Ti_2CO_2 MXene Incorporated with Neighboring Elements (Sc, V, B and N). *Journal of Electronic Materials* **2017**, *46*, 2460–2466.

8. Ling, Z.; Ren, C. E.; Zhao, M.-Q.; Yang, J.; Giammarco, J. M.; Qiu, J.; Barsoum, M. W.;

Gogotsi, Y. Flexible and conductive MXene films and nanocomposites with high capacitance. *Proceedings of the National Academy of Sciences* **2014**, *111*, 16676–16681.

9. Tang, Q.; Zhou, Z.; Shen, P. Are MXenes Promising Anode Materials for Li Ion Batteries? Computational Studies on Electronic Properties and Li Storage Capability of Ti_3C_2 and $Ti_3C_2X_2$ (X = F, OH) Monolayer. *Journal of the American Chemical Society* **2012**, *134*, 16909–16916, PMID: 22989058.

10. Siriwardane, E. M. D.; Demiroglu, I.; Sevik, C.; Çakırda, D. Achieving Fast Kinetics and Enhanced Li Storage Capacity for $Ti_3C_2O_2$ by Intercalation of Quinone Molecules. *ACS Appl. Energy Mater.* **2019**, *2*, 1251–1258.

11. Siriwardane, E. M. D.; Çakır, D. Enhanced Electrochemical Storage Properties of Na- and Mg-Intercalated B-Doped-Graphene Based Heterostructures and Bilayers. *The Journal of Physical Chemistry C* **2020**, *124*, 1260–1268.

12. Kamysbayev, V.; Filatov, A. S.; Hu, H.; Rui, X.; Lagunas, F.; Wang, D.; Klie, R. F.; Talapin, D. V. Covalent surface modifications and superconductivity of two-dimensional metal carbide MXenes. *Science* **2020**,

13. Wang, Y.; Zhou, M.; Xu, L.-C.; Zhao, W.; Li, R.; Yang, Z.; Liu, R.; Li, X. Achieving superior high-capacity batteries with the lightest Ti2C MXene anode by first-principles calculations: Overarching role of S-functionate (Ti_2CS_2) and multivalent cations carrier. *Journal of Power Sources* **2020**, *451*, 227791.

14. Xie, Y.; Dall'Agnese, Y.; Naguib, M.; Gogotsi, Y.; Barsoum, M. W.; Zhuang, H. L.; Kent, P. R. C. Prediction and Characterization of MXene Nanosheet Anodes for Non-Lithium-Ion Batteries. *ACS Nano* **2014**, *8*, 9606–9615, PMID: 25157692.

15. Meng, Q.; Ma, J.; Zhang, Y.; Li, Z.; Zhi, C.; Hu, A.; Fan, J. The S-functionalized Ti_3C_2 Mxene as a high capacity electrode material for Na-ion batteries: a DFT study. *Nanoscale* **2018**, *10*, 3385–3392.

16. Lee, S.; Jung, S. C.; Han, Y.-K. Fe_2CS_2 MXene: a promising electrode for Al-ion batteries. *Nanoscale* **2020**, *12*, 5324–5331.

17. Kresse, G.; Hafner, J. ab initio. *Phys. Rev. B* **1993**, *47*, 558–561.

18. Kresse, G.; Hafner, J. ab initio. *Phys. Rev. B* **1994**, *49*, 14251–14269.

19. G. Kresse, J. F. Efficiency of ab initio Total Energy Calculations for Metals and Semiconductors Using a Plane-Wave Basis Set. *Comput. Mater. Sci.* **1996**, *6*, 15–50.

20. Kresse, G.; Furthmüller, J. Efficient Iterative Schemes for ab initio Total-Energy Calculations Using a Plane-Wave Basis Set. *Phys. Rev. B* **1996**, *54*, 11169–11186.

21. Blöchl, P. E. Projector Augmented-Wave Method. *Phys. Rev. B* **1994**, *50*, 17953–17979.

22. Kresse, G.; Joubert, D. From Ultrasoft Pseudopotentials to the Projector Augmented-Wave Method. *Phys. Rev. B* **1999**, *59*, 1758–1775.

23. Perdew, J. P.; Burke, K.; Ernzerhof, M. Generalized Gradient Approximation Made Simple. *Phys. Rev. Lett.* **1996**, *77*, 3865–3868.

24. Perdew, J. P.; Burke, K.; Ernzerhof, M. Generalized Gradient Approximation Made Simple [Phys. Rev. Lett. 77, 3865 (1996)]. *Phys. Rev. Lett.* **1997**, *78*, 1396–1396.

25. Togo, A.; Tanaka, I. First principles phonon calculations in materials science. *Scr. Mater.* **2015**, *108*, 1–5.

26. Henkelman, G.; Uberuaga, B. P.; Jónsson, H. A Climbing Image Nudged Elastic Band Method for Finding Saddle Points and Minimum Energy Paths. *J. Chem. Phys.* **2000**, *113*, 9901–9904.

27. Henkelman, G.; Jónsson, H. Improved Tangent Estimate in the Nudged Elastic Band Method for Finding Minimum Energy Paths and Saddle Points. *J. Chem. Phys.* **2000**, *113*, 9978–9985.

28. Gouveia, J. D.; Viñes, F.; Illas, F.; Gomes, J. R. B. MXenes atomic layer stacking phase transitions and their chemical activity consequences. *Phys. Rev. Materials* **2020**, *4*, 054003.

29. Wang, Y.; Shen, J.; Xu, L.-C.; Yang, Z.; Li, R.; Liu, R.; Li, X. Sulfur-functionalized vanadium carbide MXene (V_2CS_2) as a promising anchoring material for lithium–sulfur batteries. *Phys. Chem. Chem. Phys.* **2019**, *21*, 18559–18568.

30. Mehta, V.; Saini, H. S.; Srivastava, S.; Kashyap, M. K.; Tankeshwar, K. S-Functionalized Mo_2C Monolayer as a Novel Electrode Material in Li-Ion Batteries. *The Journal of Physical Chemistry C* **2019**, *123*, 25052–25060.

31. Gandi, A. N.; Alshareef, H. N.; Schwingenschlögl, U. Thermoelectric Performance of the MXenes M_2CO_2(M = Ti, Zr, or Hf). *Chemistry of Materials* **2016**, *28*, 1647–1652.

32. Champagne, A.; Shi, L.; Ouisse, T.; Hackens, B.; Charlier, J.-C. Electronic and vibrational properties of V_2C-based MXenes: From experiments to first-principles modeling. *Phys. Rev. B* **2018**, *97*, 115439.

33. Sun, X.; Gao, Y.; Zhao, C.; Deng, S.; Zhong, X.; Zhuang, G.; Wei, Z.; Wang, J.-g. Palladium Dimer Supported on Mo_2CO_2(MXene) for Direct Methane to Methanol Conversion. *Advanced Theory and Simulations* **2018**, *2*, 1800158.

34. Shannon, R. D. Revised effective ionic radii and systematic studies of interatomic distances in halides and chalcogenides. *Acta Crystallographica Section A* **1976**, *32*, 751–767.

35. Morales-García, n.; Mayans-Llorach, M.; Viñes, F.; Illas, F. Thickness biased capture of CO2 on carbide MXenes. *Phys. Chem. Chem. Phys.* **2019**, *21*, 23136–23142.

36. Viñes, F.; Sousa, C.; Liu, P.; Rodriguez, J. A.; Illas, F. A systematic density functional theory study of the electronic structure of bulk and (001) surface of transition-metals carbides. *The Journal of Chemical Physics* **2005**, *122*, 174709.

37. Grimme, S.; Antony, J.; Ehrlich, S.; Krieg, H. A consistent and accurate ab initio parametrization of density functional dispersion correction (DFT-D) for the 94 elements H-Pu. *The Journal of Chemical Physics* **2010**, *132*, 154104.

38. van de Walle, A. Multicomponent multisublattice alloys, nonconfigurational entropy and other additions to the Alloy Theoretic Automated Toolkit. *Calphad* **2009**, *33*, 266–278.

39. van de Walle, A.; Asta, M. D.; Ceder, G. The Alloy Theoretic Automated Toolkit: A User Guide. *Calphad* **2002**, *26*, 539–553.

40. van de Walle, A.; Ceder, G. Automating First-Principles Phase Diagram Calculations. *J. Phase Equilib.* **2002**, *23*, 348–359.

41. Parrinello, M.; Rahman, A. Crystal Structure and Pair Potentials: A Molecular-Dynamics Study. *Phys. Rev. Lett.* **1980**, *45*, 1196–1199.

42. Parrinello, M.; Rahman, A. Polymorphic transitions in single crystals: A new molecular dynamics method. *Journal of Applied Physics* **1981**, *52*, 7182–7190.

43. Kurahashi, S.; Arabnejad, S.; Ushiyama, H.; Yamashita, K. Li and Na Interaction with Ti_2C-MXene: A First-Principles Calculation. *Journal of Computer Chemistry, Japan* **2019**, *18*, 84–94.

44. Çakır, D.; Sevik, C.; Gülseren, O.; Peeters, F. M. Mo2C as a high capacity anode material: a first-principles study. *J. Mater. Chem. A* **2016**, *4*, 6029–6035.

45. Eames, C.; Islam, M. S. Ion Intercalation into Two-Dimensional Transition-Metal Carbides: Global Screening for New High-Capacity Battery Materials. *Journal of the American Chemical Society* **2014**, *136*, 16270–16276, PMID: 25310601.

46. Xie, Y.; Naguib, M.; Mochalin, V. N.; Barsoum, M. W.; Gogotsi, Y.; Yu, X.; Nam, K.-W.; Yang, X.-Q.; Kolesnikov, A. I.; Kent, P. R. C. Role of Surface Structure on Li-Ion

Energy Storage Capacity of Two-Dimensional Transition-Metal Carbides. *Journal of the American Chemical Society* **2014**, *136*, 6385–6394, PMID: 24678996.

47. Zhao, T.; Zhang, S.; Guo, Y.; Wang, Q. TiC_2: a new two-dimensional sheet beyond MXenes. *Nanoscale* **2016**, *8*, 233–242.

48. Li-ion battery materials: present and future. *Materials Today* **2015**, *18*, 252 – 264.

49. Shukla, V.; Jena, N. K.; Naqvi, S. R.; Luo, W.; Ahuja, R. Modelling high-performing batteries with Mxenes: The case of S-functionalized two-dimensional nitride Mxene electrode. *Nano Energy* **2019**, *58*, 877 – 885.

50. Zhu, J.; Chroneos, A.; Eppinger, J.; Schwingenschlögl, U. S-functionalized MXenes as electrode materials for Li-ion batteries. *Applied Materials Today* **2016**, *5*, 19 – 24.

51. Yang, Z.; Choi, D.; Kerisit, S.; Rosso, K.; Wang, D.; Zhang, J.; Graff, G.; Liu, J. Nanostructures and lithium electrochemical reactivity of lithium titanites and titanium oxides: A review. *Journal of Power Sources* **2009**, *192*, 588–598.

52. Lunell, S.; Stashans, A.; Ojamäe, L.; Lindström, H.; Hagfeldt, A. Li and Na Diffusion in TiO2 from Quantum Chemical Theory versus Electrochemical Experiment. *Journal of the American Chemical Society* **1997**, *119*, 7374–7380.

53. Pumera, M.; Sofer, Z.; Ambrosi, A. Layered transition metal dichalcogenides for electrochemical energy generation and storage. *J. Mater. Chem. A* **2014**, *2*, 8981–8987.

54. Peng, L.; Zhu, Y.; Chen, D.; Ruoff, R. S.; Yu, G. Two-Dimensional Materials for Beyond-Lithium-Ion Batteries. *Advanced Energy Materials* **2016**, *6*, 1600025.

55. Ataca, C.; Şahin, H.; Ciraci, S. Stable, Single-Layer MX2 Transition-Metal Oxides and Dichalcogenides in a Honeycomb-Like Structure. *The Journal of Physical Chemistry C* **2012**, *116*, 8983–8999.

56. Rasmussen, F. A.; Thygesen, K. S. Computational 2D Materials Database: Electronic Structure of Transition-Metal Dichalcogenides and Oxides. *The Journal of Physical Chemistry C* **2015**, *119*, 13169–13183.

57. Whittingham, M. S. Lithium Batteries and Cathode Materials. *Chemical Reviews* **2004**, *104*, 4271–4302, PMID: 15669156.

58. Aierken, Y.; Sevik, C.; Gülseren, O.; Peeters, F. M.; Çakır, D. MXenes/graphene heterostructures for Li battery applications: a first principles study. *J. Mater. Chem. A* **2018**, *6*, 2337–2345.

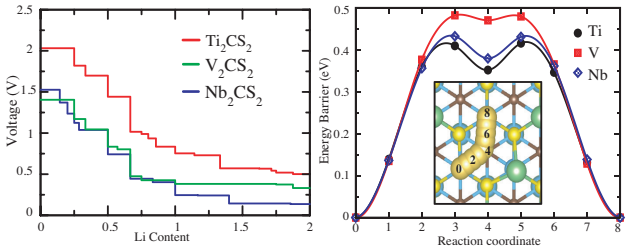

Table of content figure.